

Outflow of hot and cold molecular gas from the obscured secondary nucleus of NGC 3256: closing in on feedback physics

B. H. C. Emonts^{1*}, J. Piqueras-López¹, L. Colina¹, S. Arribas¹, M. Villar-Martín¹, M. Pereira-Santaella^{1,2}, S. Garcia-Burillo³, and A. Alonso-Herrero⁴

¹ Centro de Astrobiología (INTA-CSIC), Ctra de Torrejón a Ajalvir, km 4, 28850 Torrejón de Ardoz, Madrid, Spain
e-mail: bjornemonts@gmail.com

² Istituto di Astrofisica e Planetologia Spaziali (INAF), Via Fosso del Cavaliere 100, I-00133 Roma, Italy

³ Observatorio Astronómico Nacional (OAN), Observatorio de Madrid, Alfonso XII, 3, 28014, Madrid, Spain

⁴ Instituto de Física de Cantabria (CSIC-UC), 39005 Santander, Spain

ABSTRACT

The nuclei of merging galaxies are often deeply buried in dense layers of gas and dust. In these regions, gas outflows driven by starburst and active galactic nuclear activity are believed to play a crucial role in the evolution of these galaxies. However, to fully understand this process it is essential to resolve the morphology and kinematics of such outflows. Using near-infrared integral-field spectroscopy obtained with SINFONI on the Very Large Telescope, we detect a kpc-scale structure of high-velocity molecular hydrogen (H_2) gas associated with the deeply buried secondary nucleus of the infrared-luminous merger-galaxy NGC 3256. We show that this structure is most likely the hot component of a molecular outflow, which is detected also in the cold molecular gas by Sakamoto et al. This outflow, with a total molecular gas mass of $M_{H_2} \sim 2 \times 10^7 M_\odot$, is among the first to be spatially resolved in both the hot molecular H_2 gas with VLT/SINFONI and the cold molecular CO emitting gas with ALMA. The hot and cold components share a similar morphology and kinematics, with a hot-to-cold molecular gas mass ratio of $\sim 6 \times 10^{-5}$. The high (~ 100 pc) resolution at which we map the geometry and velocity structure of the hot outflow reveals a biconical morphology with opening angle $\sim 40^\circ$ and gas spread across a FWZI ~ 1200 km s^{-1} . Because this collimated outflow is oriented close to the plane of the sky, the molecular gas may reach maximum intrinsic outflow velocities of ~ 1800 km s^{-1} , with an average mass outflow rate of at least $\dot{M}_{\text{outfl}} \sim 20 M_\odot \text{ yr}^{-1}$. By modeling the line-ratios of various near-infrared H_2 transitions, we show that the H_2 -emitting gas in the outflow is heated through shocks or X-rays to a temperature of $T \sim 1900 \pm 300$ K. The energy needed to drive the collimated outflow is most likely provided by a hidden Compton-thick AGN or by the nuclear starburst. We show that the global kinematics of the molecular outflow that we detect in NGC 3256 mimic those of CO-outflows that have been observed at much lower spatial resolution in starburst- and active galaxies.

Key words. galaxies: NGC 3256 – galaxies: starburst – galaxies: active – galaxies: nuclei – ISM: jets, outflows – ISM: dust, extinction

1. Introduction

Luminous and ultra-luminous infrared galaxies, also called LIRGs ($L_{\text{IR}} > 10^{11} L_\odot$) and ULIRGs ($L_{\text{IR}} > 10^{12} L_\odot$), are galaxies with massive dust-enshrouded star formation and often a deeply buried active galactic nucleus (AGN; Sanders & Mirabel 1996). Because (U)LIRGs can be found at relatively low z , they are excellent laboratories for studying physical processes that are crucial in the evolution of massive galaxies, from galaxy merging to starburst/AGN-induced feedback. These processes, in particular when they occur in the nuclei, are often hidden behind thick layers of gas and dust, which absorb most of the light before re-radiating it at IR wavelengths.

Integral-field spectroscopy in the near infrared (IR) provides an excellent tool to study the physical processes in the central regions of (U)LIRGs. At near-IR wavelengths the dust extinction is much lower than in the optical. In addition, in the near-IR a variety of emission lines from different gas phases, as well as stellar absorption lines, can often be observed simultaneously (from coronal [Si VI] and ionized Br γ or Pa α to partially ionized [Fe II] and molecular H_2 emission). Particularly interesting is that a range of near-IR transitions of H_2 can be targeted to study the physical properties of the molecular gas. Another in-

trinsic advantage of near-IR integral-field spectroscopy is that, apart from being able to image the gas at high spatial resolution, different gas structures can also be distinguished kinematically. This can be done in detail by decomposing complex line profiles into multiple kinematic components across the field of view of the spectrograph.

The strength of a detailed kinematic analysis of near-IR integral-field spectra was recently shown by Rupke & Veilleux (2013), who revealed the base of a deeply buried H_2 outflow in the nearby quasi-stellar object QSO F08572+3915. Other observational techniques have also revealed evidence that links nuclear AGN and starburst activity with heating and outflow of neutral and molecular gas in low- z galaxies (Oosterloo et al. 2000; Leon et al. 2007; Feruglio et al. 2010; Alatalo et al. 2011; Rupke & Veilleux 2011; Aalto et al. 2012; Guillard et al. 2012; Dasyra & Combes 2012; Combes et al. 2013; Morganti et al. 2005, 2013a,b; Mahony et al. 2013; Dasyra et al. 2014; Garcia-Burillo et al. 2014; Cazzoli et al. 2014; Tadhunter et al. 2014). Moreover, recent surveys with instruments like Herschel and the Plateau de Bure Interferometer revealed evidence of massive outflows of molecular gas in ULIRGs (e.g., Chung et al. 2011; Sturm et al. 2011; Spoon et al. 2013; Veilleux et al. 2013; Cicone et al. 2014), which complement extensively studied ionized gas outflows in these systems (e.g., Heckman et al. 1990;

* Marie Curie Fellow

Westmoquette et al. 2012; Bellocchi et al. 2013; Rodríguez Zaurín et al. 2013; Arribas et al. 2014). Thus, if feedback onto the molecular gas is common in merger systems with dust-obscured starburst/AGN cores, we expect to find evidence of this through detailed 3D kinematic studies of the near-IR H₂ lines in other nearby IR-luminous galaxies.

In this paper, we perform a kinematic and morphological analysis of the near-IR H₂ emission from molecular gas associated with the deeply buried secondary nucleus of NGC 3256, which is the most luminous LIRG within $z < 0.01$ ($L_{\text{IR}} \sim 5 \times 10^{11} L_{\odot}$; Sanders et al. 2003). In Piqueras López et al. (2012a) we previously revealed that NGC 3256 contains a large-scale rotating H₂ disk, which we imaged by tracing the H₂ 1-0S(1) $\lambda=2.12\mu\text{m}$ line with near-IR integral-field data from the *Spectrograph for Integral Field Observations in the Near Infrared at the Very Large Telescope* (VLT/SINFONI; Eisenhauer et al. 2003; Bonnet et al. 2004). However, the standard single-Gaussian fitting procedure that we applied in Piqueras López et al. (2012a) revealed residuals that suggested the presence of more complex kinematics across various regions (see Sect. 2). We further explore the complex kinematics of the H₂ gas in NGC 3256 in this paper.

1.1. NGC 3256

NGC 3256 is a gas-rich merger with prominent tidal tails, galactic winds and ionized gas outflows (e.g., Scarrott et al. 1996; Moran et al. 1999; Heckman et al. 2000; Lípari et al. 2000, 2004; English et al. 2010; Monreal-Ibero et al. 2010; Rich et al. 2011; Leitherer et al. 2013; Bellocchi et al. 2013; Arribas et al. 2014). It contains two nuclei, separated by ~ 1 kpc. The secondary, or southern, nucleus is heavily obscured, as revealed with IR and radio observations (Norris & Forbes 1995; Kotilainen et al. 1996; Alonso-Herrero et al. 2006a; Lira et al. 2008; Díaz-Santos et al. 2008). Various authors have claimed that this secondary nucleus may host a heavily obscured AGN (e.g., Kotilainen et al. 1996; Neff et al. 2003). So far, X-ray studies provided inconclusive evidence for this (Lira et al. 2002; Jenkins et al. 2004; Pereira-Santaella et al. 2011), while the near- and mid-IR properties of both nuclei are ascribed mostly to star-formation activity (Alonso-Herrero et al. 2006b; Lira et al. 2008; Pereira-Santaella et al. 2010; Alonso-Herrero et al. 2012).

Molecular gas was detected through observations of H₂ and various tracers of cold molecular gas (e.g., Moorwood & Oliva 1994; Doyon et al. 1994; Sargent et al. 1989; Mirabel et al. 1990; Aalto et al. 1991; Casoli et al. 1992; Baan et al. 2008). Sakamoto et al. (2006) used CO(2-1) observations taken with the Submillimeter Array (SMA) to map a large ($r > 3$ kpc) disk of cold molecular gas rotating about the mid-point between the two nuclei. Part of this disk was also mapped in H₂ (Piqueras López et al. 2012a) and H α (Lípari et al. 2000; Rodríguez-Zaurín et al. 2011; Bellocchi et al. 2013). Sakamoto et al. (2006) also found a high-velocity component of molecular gas. In a concurrent paper, Sakamoto et al. (2014) present new ALMA data that reveal that the high-velocity molecular gas is associated with two outflows, namely a starburst-driven superwind from the primary nucleus and a much more collimated kpc-scale bipolar outflow from the secondary nucleus. Our VLT/SINFONI H₂ data reveal independent evidence of this collimated bipolar outflow and will shed a new light on its nature.

Throughout this paper, we assume $z = 0.009354$ (which is the redshift of the Br γ peak emission at the location of the secondary nucleus) and $D = 44.6$ Mpc ($1'' = 216$ pc), as per Piqueras López et al. (2012a).

2. Data

We use near-IR data obtained with VLT/SINFONI previously presented in Piqueras López et al. (2012a), with pixel-size $0.125''$, seeing $\sim 0.6''$, spectral resolution $6.0 \pm 0.6 \text{ \AA}$ and dispersion 2.45 \AA/pixel . These data originally revealed a large-scale H₂ disk (Sect. 1), which is also shown in our Fig. 1. From visual inspection, the single Gaussian fit previously applied to the H₂ 1-0S(1) emission line by Piqueras López et al. (2012a) did not produce satisfactory results for mapping the full kinematic structure of the hot molecular gas. This was most notable in the regions ~ 2.5 arcsec south and ~ 3.5 arcsec north of the secondary nucleus in Piqueras López et al. (2012a), where the measured velocity from the Gaussian fit to the H₂ 1-0S(1) line did not reflect the otherwise regular rotation pattern of the large-scale H₂ disk. For the current work, we modified the data analysis routine used by Piqueras López et al. (2012a) to fit two Gaussian components to the H₂ line profile there where required. This routine was compiled for the Interactive Data Language (IDL) and uses the MPFIT package for the χ^2 minimization (Markwardt 2009). No constraints were placed on the fitting parameters and all fits were visually inspected to ensure their validity. A flux (F), velocity (v) and velocity dispersion (σ) map (corrected for instrumental broadening) were created for each component, and boxcar-smoothed by 3 pixels in both spatial directions.

We also used archival ALMA cycle-0 data to compare the morphology and kinematics of certain H₂ features with those observed in CO(3-2) (program 2011.0.00525; PI K. Sakamoto, see also Sakamoto 2013a,b). These data have a spatial resolution of $1.2'' \times 0.7''$ (PA = 23°) and channel width of 10 km s^{-1} , with the standard ALMA archival pipeline-reduction applied. In a concurrent paper, Sakamoto et al. (2014) present these CO data (and other molecular gas tracers) using additional calibration and analysis techniques, hence we refer to their work for further details on the CO properties of NGC 3256.

Images of the Hubble Space Telescope *Near Infrared Camera and Multi-Object Spectrometer 2* (HST/NICMOS2) filters F160W, F212N and F237M (prog. ID 7251, PI: J. Black; see also Rossa et al. 2007) and the *Wide Field and Planetary Camera 2* (HST/WFPC2) filter F814W (prog. ID 5369, PI: S. Zepf; see also Zepf et al. 1999, Laine et al. 2003) were extracted through the Hubble Legacy Archive. Our SINFONI data were overlaid onto these HST images by visually matching the coordinates to those of the secondary nucleus in the HST/NICMOS2 data.

3. Results

3.1. Hot molecular structure

The results of mapping the H₂ 1-0S(1) line with two Gaussian components are shown in Fig. 1. A “narrow” component is visible across the field of view (F.o.V.), tracing the large-scale rotating molecular gas disk previously discussed by Piqueras López et al. (2012a). A second, “broad” component is detected in three regions (A, B and C in Fig. 1). Properties of the broad-component emission are given in Table 1.

The most prominent broad-component features are the bright, blue-shifted structure A (projected distance ~ 440 pc south of the secondary nucleus) and the redshifted structure B (~ 800 pc north of the secondary nucleus). The integrated intensity is $I = 4.2$ and $3.8 \times 10^{-15} \text{ erg s}^{-1} \text{ cm}^{-2}$ across regions A and B, respectively. This H₂ gas has velocities that appear to be decoupled from those of the main narrow-component disk and shows a significantly higher velocity dispersion than the disk emission.

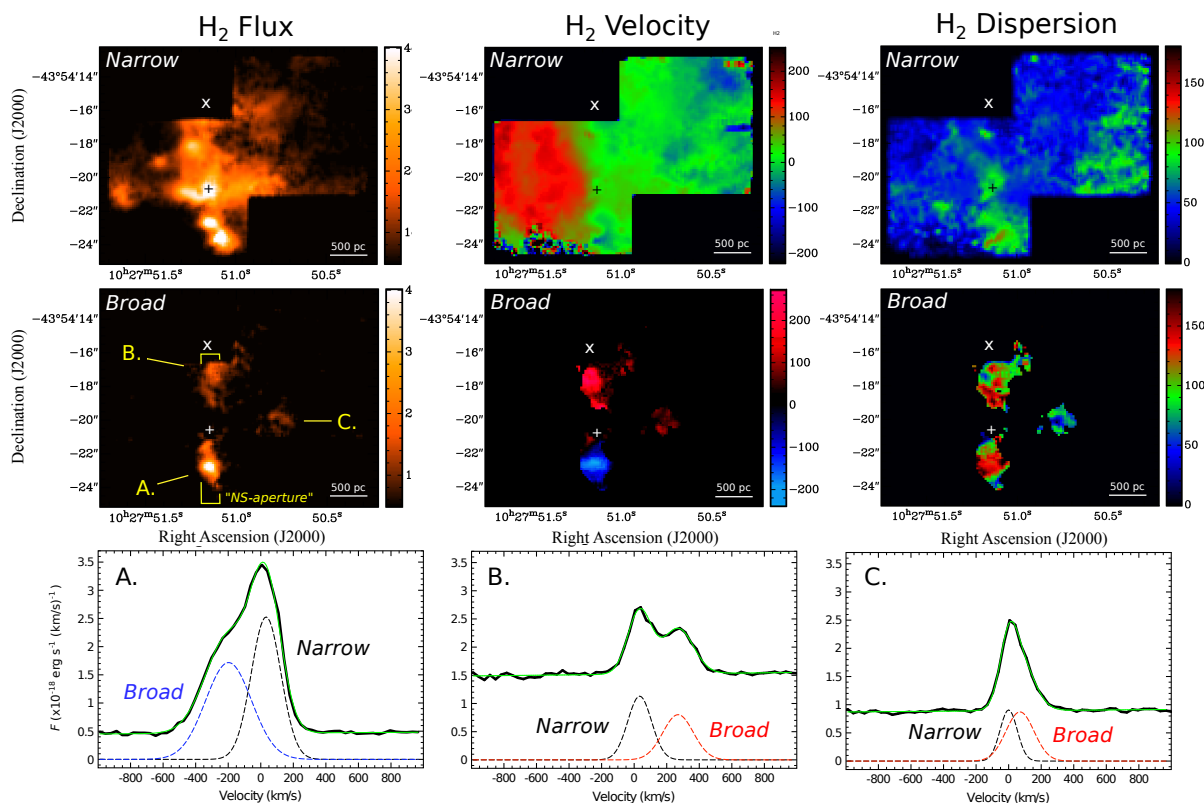


Fig. 1. SINFONI view of the H_2 emission in NGC 3256, mostly covering the region surrounding the secondary (southern) nucleus. The primary and secondary nucleus are marked with an \times and $+$, respectively, and are shown in more detail in Fig. 3. *Top + middle:* Maps of the H_2 flux (F), velocity of the emission-line peak (v) and velocity dispersion ($\sigma = \text{FWHM}/2.35$, with FWHM the full width at half the maximum intensity) of both the narrow- (*top*) and broad-component gas (*middle*). Velocities are with respect to $z = 0.009354$ as per Piqueras López et al. (2012a), which is the assumed systemic velocity of the secondary core (Sect. 1.1). Units are in $\times 10^{-17} \text{ erg s}^{-1} \text{ cm}^{-2}$ (F) and km s^{-1} (v and σ). *Bottom:* H_2 emission-line profiles, plus continuum-subtracted 2-component Gaussian fit, in regions A, B and C. The spectra were extracted from a circular aperture of 13 spaxels of $0.125'' \times 0.125''$ each (i.e., roughly the size of the seeing disk), centered on the broad-component H_2 features.

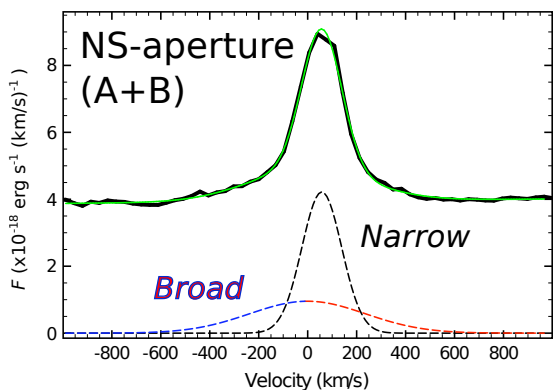


Fig. 2. Integrated H_2 emission-line profile across the combined $1.1'' \times 8.8''$ north-south aperture that covers the full broad-component A+B region (as visualized in the *middle-left* panel of Fig. 1). The 0-velocity is defined as the redshift of the $\text{Br}\gamma$ peak-emission at the location of the secondary nucleus. The $\sim 60 \text{ km s}^{-1}$ redshift of the narrow component is likely due to the fact that the kinematic center of the large-scale molecular disk is $\sim 500 \text{ pc}$ north of the secondary nucleus.

When this broad component is integrated across the full extent of regions A+B, it appears to be centered both spatially and kinematically around the secondary nucleus. The corresponding integrated broad-component profile shown in Fig. 2 covers a total full-width-at-zero-intensity velocity range of $\text{FWZI}_{\text{tot}} \approx 1200 \text{ km s}^{-1}$ (or $\text{FWHM}_{\text{tot}} \sim 560 \text{ km s}^{-1}$) and is symmetric with re-

spect to our assumed systemic velocity of the secondary nucleus. We note that our SINFONI F.o.V. does not cover the primary nucleus (north of region B), while the line-fitting south of region A becomes too uncertain (Fig. 1 *top-middle*), hence the full extent of the broad-component H_2 structure may not be revealed.

Figure 3 shows a contour map of the broad-component H_2 emission overlaid onto various optical and near-IR HST images. The 3-color composite HST/NICMOS F160W+H212N+F237M image in Fig. 3 (*middle*) shows a distinctive red feature at the location of the bright H_2 emission in region A. As shown on the right of Fig. 3, this red feature (marked with an arrow) only appears in the NICMOS F237M filter. The F237M filter ($2.29 - 2.44 \mu\text{m}$) includes the H_2 1-0Q(1), 1-0Q(2) and 1-0Q(3) emission lines at the redshift of NGC 3256, of which the prominent Q(1) and Q(2) lines fall within the wavelength range of our SINFONI data.¹ The same red feature does not appear in the F160W and F212N filters that mostly trace the near-IR continuum. We thus believe that the red feature south of the secondary nucleus in the NICMOS image consists of molecular line emission, which we also see as enhanced H_2 emission in both the narrow and broad component in region A (Fig. 1). No obvious features are visible in any of the NICMOS filters in region B. We also find no obvious stellar or dusty counterpart that follows the broad-component H_2 emission across regions A and B in optical wide-band HST/WFPC2 imaging (Fig. 3 - *left*), although a dark line

¹ Because of residual sky-line effects at the very edge of the SINFONI wavelength coverage, we could not do an accurate spectral analysis of the H_2 1-0Q(1) and H_2 1-0Q(2) lines.

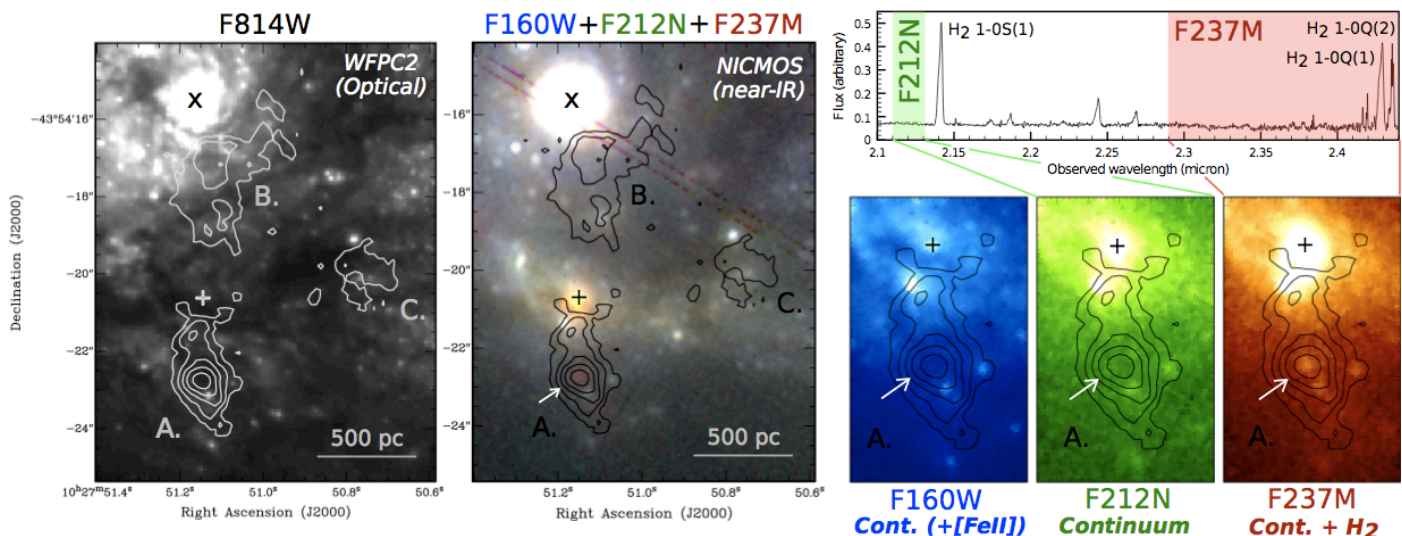


Fig. 3. *Left:* Contours of the broad-component H₂ emission from Fig. 1 (levels: 0.7, 1.3, 2.0, 2.8, 4.0 × 10⁻¹⁷ erg s⁻¹ cm⁻²) overlaid onto an optical image taken with the HST/WFPC2 F814W_{724–878 nm} wide-band filter. *Middle:* Contours of the broad-component H₂ emission overlaid onto a 3-color near-IR image of the same region taken with the HST/NICMOS2 (filters: blue = F160W_{1.4–1.8 μm}, green = F212N_{2.111–2.132 μm}, red = F237M_{2.29–2.44 μm}). *Top right:* VLT/SINFONI spectrum obtained against the region of peak H₂ emission in region A (aperture 13 pixels). Visualized are the regions of the HST/NICMOS F212N narrow-band (2.111–2.132 μm) and F237M medium-band filter (2.29–2.44 μm). The F237M filter includes the prominent H₂ 1-0 Q(1) and Q(2) lines. The F160W wide-band filter (1.4–1.8 μm) covers the VLT/SINFONI H-band spectrum of this object, with [Fe II] as the most prominent emission-line in this spectral region (see Piqueras López et al. 2012a). *Right bottom:* Region A as observed in the three different NICMOS filters. The arrows point to the region with enhanced H₂ emission in both the VLA/SINFONI and HST/NICMOS F237M data.

does appear to cross the region of peak H₂ brightness (at least in projection). In addition, the Bry-line of ionized gas in our SINFONI data is very weak in region A and does not have a prominent broad component in region B. It should be noted that the weak Bry does appear to have an increased velocity dispersion in region A (Piqueras López et al. 2012a), while a weak broad-component feature in H α has been reported south of region A by Bellocchi et al. (2013). Nevertheless, the broad component features in regions A and B appear to *predominantly consist of molecular gas*.

A faint reservoir of redshifted H₂ is also seen in region C. This gas has σ similar to that of the narrow-component disk, while the velocity shift between the narrow and broad component is much smaller than for regions A and B. This makes it difficult to perform an in-depth analysis of the H₂ emission in region C (as will become clear also from Fig. A.1). Moreover, the broad-component emission in region C is found along a prominent tidal arm in the NICMOS F237M data (Fig. 3) and Piqueras López (2014) shows that – unlike regions A and B – region C coincides with a starforming region with bright Bry emission. In this paper we will therefore only present the basic H₂ results for region C, while a more detailed analysis of the near-IR emission-line properties in this and other starforming regions in nearby (U)LIRGs is left for a future paper (Piqueras et al in prep).

Apart from the H₂ 1-0 S(1) 2.12 μm line, we see a broad component also in other H₂ lines, namely H₂ 1-0 S(0) 2.22 μm, 1-0 S(2) 2.03 μm, 1-0 S(3) 1.96 μm, 2-1 S(1) 2.25 μm, 2-1 S(2) 2.15 μm and 2-1 S(3) 2.07 μm. For all H₂ transitions we performed a kinematic analysis similar to that of the 1-0 S(1) line. Details of this procedure, as well as the line profiles and resulting line fluxes, are provided in Appendix A.

Table 1. Physical parameters of the broad-component H₂ 1-0S(1) features. I is the integrated intensity of the H₂ emission. Δv_{peak} is the maximum velocity of the peak of the broad component with respect to $z = 0.009354$ across each region. σ_{max} is the maximum velocity dispersion of the gas, corresponding to $\sigma \equiv \text{FWHM}/(2\sqrt{2\ln(2)})$, with FWHM the full width at half the maximum intensity of the broad component. The maximum values have been obtained from the images shown in Fig. 1.

	Region A.	Region B.	Region C.
I (× 10 ⁻¹⁵ erg s ⁻¹ cm ⁻²)	4.2	3.8	1.1
Δv_{peak} (km s ⁻¹)	-240	+270	+110
σ_{max} (km s ⁻¹)	190	180	100
FWHM _{max} (km s ⁻¹)	447	424	235

3.1.1. Temperature and excitation mechanism

The relative intensities of the various H₂ transitions can be used to discriminate between the various mechanisms that excite the H₂ gas, and to estimate the gas temperature. Models show that H₂ can be excited either through thermal processes, such as shocks or UV/X-ray radiation, or non-thermal processes like UV-fluorescence (e.g., Lepp & McCray 1983; Hollenbach & McKee 1989; Sternberg & Dalgarno 1989; Brand et al. 1989; Draine & Woods 1990; Maloney et al. 1996; Dors et al. 2012; Black & van Dishoeck 1987). In case of thermal processes, the H₂ levels are excited through inelastic collisions, resulting in gas that is approximately in Local Thermal Equilibrium (LTE). For gas in LTE the various H₂ line ratios can be fitted by a single excitation-temperature model (see, e.g., Davies et al. 2003). In the case of non-thermal excitation, absorption of UV photons with $\lambda > 912\text{\AA}$ is followed by a fluorescent cascade of electrons through the vibrational and rotational levels of the ground state. In this case, even though in most environments the lowest vibrational levels of H₂ ($v = 1$) are still well thermalized, the higher level transitions are significantly stronger than expected based

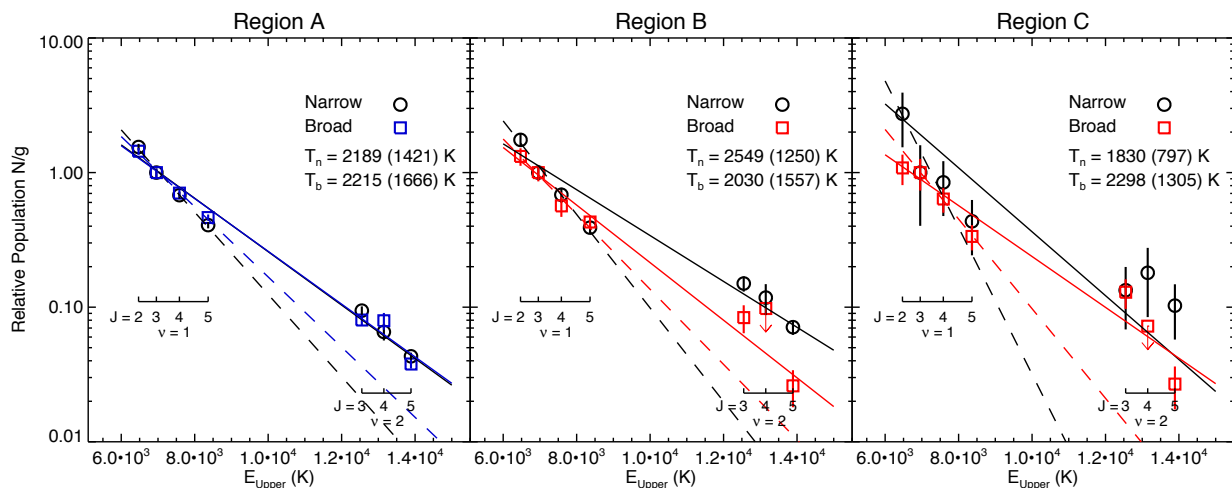


Fig. 4. Modeling the relative population levels of the H_2 transitions using single excitation-temperature LTE models (see Davies et al. 2003). The relative population levels have been derived from the intensities of the H_2 transitions listed in Table A.1. The circles and squares represent the narrow and broad component, respectively. The solid lines show the single-temperature fits using both the $\nu = 1$ and $\nu = 2$ transitions (i.e., assuming fully thermalized LTE gas conditions). The dashed lines show the single-temperature fits to only the $\nu = 1$ transitions (i.e., taking into consideration that the $\nu = 2$ transitions could be over-populated compared to fully thermalized LTE conditions). The best-fit temperatures for the narrow (n) and broad (b) component in the various regions are also show (with in brackets the temperature derive from the fit to only the $\nu = 1$ transitions).

on single-temperature LTE models and more complex models are required to derive the gas temperature (Davies et al. 2003).

To estimate the excitation temperature of the H_2 -emitting gas, we fit LTE models to the relative population levels across the range of H_2 transitions for the various components (see Appendix A). As can be seen in Fig. 4, if a single-temperature model is fitted to both the $\nu = 1$ and $\nu = 2$ transitions, we derive an estimated temperature of $T \sim 2000 - 2200$ K. A fit to only the $\nu = 1$ transitions renders a temperature of $T \sim 1600$ K, in which case the $\nu = 2$ transitions are slightly over-populated. This indicates that the excitation conditions of the broad-component H_2 gas may be somewhat more complex than single-temperature LTE conditions, with non-thermal processes adding to the gas excitation, multiple gas temperature components, or a low-density, sub-thermally excited gas phase mixed with denser LTE-gas. However, our coverage of only the $\nu = 1$ and $\nu = 2$ transitions, of which the $\nu = 2$ lines are relatively weak (Fig. A.1), does not allow us to constrain the model-fitting in great detail. Moreover, as we will see in Sect. 3.2, the broad-component emission is also seen in the cold molecular $\text{CO}(3-2)$ and $\text{CO}(1-0)$ gas with an estimated ratio that suggests that also the cold gas may be thermalized. We therefore here adopt the temperature of $T \sim 1900 \pm 300$ K for the broad-component emission-line gas in regions A and B.

The bright emission from the narrow-component H_2 disk in regions A and B shows roughly similar temperature-estimates when fitting LTE models. However, for this narrow component, the over-population of the $\nu = 2$ transitions is more prominent than for the broad-component emission, in particular in region B. This suggests that the temperatures of the narrow-component H_2 gas are more uncertain, and that the excitation conditions in parts of the large-scale disk are likely more complex, than those of the broad-component emission. However, a detailed discussion of this is beyond the scope of this paper. For both the narrow- and broad-component emission in region C the errors in the fluxes for the various transitions are too large to derive any meaningful conclusions.

We use the H_2 line ratios to further investigate the excitation-mechanism that dominates the heating of the H_2 gas. Following Mouri (1994, see also Tanaka et al. 1989), we plot the ratio of the ortho-transitions $2-1 \text{S}(1)/1-0 \text{S}(1)$ against the ratio of the para-transitions $1-0 \text{S}(2)/1-0 \text{S}(0)$, which allows us to estimate whether thermal or non-thermal processes dominate the gas excitation. The results shown in Fig. 5 indicate that the gas-heating of the various components in regions A and B is dominated by thermal processes.² More specifically, the $1-0 \text{S}(2)/1-0 \text{S}(0)$ ratio of the various components (plotted on the y-axis of Fig. 5) is consistent with models that predict that shock or X-ray processes heat the gas, rather than that the H_2 is thermally excited by UV photons (the latter would result in expected gas temperatures $T \lesssim 1000$ K; see Mouri 1994 and references therein). The $2-1 \text{S}(1)/1-0 \text{S}(1)$ ratios for both the narrow and broad component in regions A and B are clearly inconsistent with what is expected when non-thermal UV-fluorescence dominates the excitation process. Within the errors, the broad-component in both region A and B falls close to the temperature of $T \sim 2000$ K along the LTE-line expected from uniform density gas that is fully thermalized. However, the deviation from this LTE-line indicates also here that the gas excitation may be more complex than simple LTE conditions. This is most prominent for the narrow component gas in region B, which suggests that either a non-negligible fraction of H_2 excitation through non-thermal processes or a mixing of molecular gas-components with different densities may occur for the H_2 gas in the large-scale disk. These results are consistent with the more detailed level population analysis of Fig. 4 that we discussed above.

² The line ratios for the narrow and broad component in region C appear consistent with this scenario, but the large errors (Fig. 4) do not allow us to derive firm conclusions, hence region C has been omitted from Fig. 5.

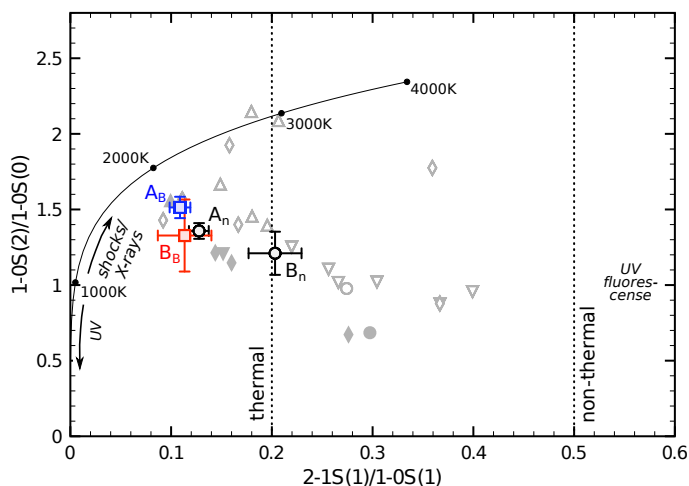


Fig. 5. H_2 line ratio diagram for the blueshifted broad component in region A (blue square), the redshifted broad component in region B (red square) and the narrow components in regions A and B (black circles). The solid black line shows the expected line ratios for uniform density gas that is in Local Thermal Equilibrium (LTE), with excitation temperatures indicated. The dotted lines provide an indication for the regions where the 2-1 S(1)/1-0 S(1) line ratio is caused by thermal (≤ 0.2) and non-thermal (≥ 0.5) conditions, based values from models that are summarized in Mouri (1994). The regions where these models predict UV photons (Sternberg & Dalgarno 1989), shocks/X-rays (Brand et al. 1989; Lepp & McCray 1983; Draine & Woods 1990; Dors et al. 2012) and UV-fluorescence (Black & van Dishoeck 1987) to dominate the gas excitation are indicated in more detail. Open gray symbols represent values from individual regions studied within other nearby galaxies (starforming regions, rings, arcs, clouds, etc.), with closed gray symbols the nuclei of these systems. Diamonds are from Mazzalay et al. (2013), downward pointing triangles from Falcón-Barroso et al. (2014), upwards pointing triangles from Bedregal et al. (2009) and circles from Piqueras López et al. (2012b). See also Ramos Almeida et al. (2009) and Riffel et al. (2013) for studies performed on integrated near-IR long-slit spectra of various types of galaxies.

3.1.2. Mass of the hot molecular gas

In Sect. 3.1.1 we showed that the H_2 level populations of the broad-component emission in regions A and B are broadly consistent with hot molecular gas at a temperature of $T \sim 1900 \pm 300$ K. This allows us to estimate the mass of the hot molecular gas following Scoville et al. (1982) and Mazzalay et al. (2013):

$$M_{\text{hot}} \simeq 5.0875 \times 10^{13} \left(\frac{D}{\text{Mpc}} \right)^2 \left(\frac{I_{1-0S(1)}}{\text{erg s}^{-1} \text{cm}^{-2}} \right) 10^{(0.4 \cdot A_{2.2})} M_{\odot}, \quad (1)$$

where D is the distance to the galaxy and $A_{2.2\mu\text{m}}$ the extinction at $2.2\mu\text{m}$. This approach assumes thermalized gas conditions and $T = 2000$ K, with a population fraction in the $(v, J) = (1, 3)$ level of $f_{(1,3)} = 0.0122$. As discussed in Sect. 3.1.1, the assumption of LTE conditions for the broad-component H_2 gas is roughly consistent to within the accuracy of our level-population analysis, although uncertainties in this remain (for example, if a fraction of the H_2 gas would be sub-thermally excited, $f_{1,3}$ would be lower and equation 1 would thus give lower limits to the H_2 mass).

According to Piqueras López et al. (2013) $A_{2.2\mu\text{m}} \approx 0.1 \times A_V$, with A_V the visual extinction. Because the broad-component H_2 emission is found outside the heavily obscured nuclei, we calculate A_V from the $\text{Br}\gamma/\text{Br}\delta$ ratio in our spectra in regions A, B and C, following Piqueras López et al. (2013). For

region B we derive $A_V = 4.3 \pm 1.3$ mag, which is close to the median $A_V = 5$ in NGC 3256 found by Piqueras López et al. (2013). For region A the $\text{Br}\gamma$ and $\text{Br}\delta$ lines are too weak to derive reliable estimates, while for region C we derive $A_V = 0.5 \pm 0.5$ mag. If we assume $A_V = 4.3$ in both region A and B, then $A_{2.2\mu\text{m}} \approx 0.1 \times A_V \sim 0.43$. Applying this $A_{2.2\mu\text{m}}$ results in a mass estimate of the hot molecular gas of $M_{\text{hot-}H_2} \sim 630$ and $570 M_{\odot}$ for the broad-component emission in region A and B, respectively. We note that when taking the strict lower limit of $A_V = 0$ in region A, the corresponding mass estimate would lower by only $\sim 33\%$.

Concluding, we estimate that the combined mass of hot molecular gas associated with the broad-component emission in regions A and B is $M_{\text{hot-}H_2} \sim 1200 M_{\odot}$.

3.2. Cold molecular counterpart

In Fig. 6 we compare our broad-component H_2 emission with high-velocity CO(3-2) gas (i.e., gas with velocities above those of the main CO disk), as observed with ALMA by Sakamoto et al. (2014). Fig. 6 illustrates that the broad-component H_2 emission of hot molecular gas in regions A and B has a counterpart in the cold molecular gas as traced by CO(3-2). The H_2 and CO show a *similar morphology and kinematics*, which are distinctly different from that of the main CO disk (which has its kinematic axis in east-west direction at position angle $\sim 75^\circ$ and inclination $\sim 30^\circ$; see Sakamoto et al. 2014 and Sect. 4.1). There could be a slight off-set between the location of the peak intensity for the H_2 and CO(3-2) emission in regions A and B, but this is within the uncertainty of our relative astrometry. No CO counterpart of the broad-component H_2 feature in region C was reliably distinguished from the main CO disk, although this is possibly due to the relatively small Δv_{peak} and σ_{max} that the broad-component molecular gas will have in this region (Table 1).

We measure CO intensities of $I_{\text{CO}(3-2)} = 23.5$ and $39.7 \text{ Jy km s}^{-1}$ in region A and B (Fig. 6). From this, we can derive mass estimates of the cold molecular gas if we know the excitation conditions of the gas. The high-velocity gas was also detected in CO(1-0) by Sakamoto et al. (2014) at lower spatial resolution. Through a basic comparison of the high-velocity component in the CO(3-2) and CO(1-0) data, we estimate that $L'_{\text{CO}(3-2)}/L'_{\text{CO}(1-0)}$ is close to unity for regions A and B, and thus broadly consistent with thermal excitation conditions. This takes into account that for region B Sakamoto et al. (2014) estimate that $\sim 34\%$ of the high-velocity CO(3-2) emission and $\sim 72\%$ of the CO(1-0) emission is contaminated by a CO outflow originating from the primary nucleus. If we assume $L'_{\text{CO}(3-2)}/L'_{\text{CO}(1-0)} = 1$ and we exclude the $\sim 34\%$ contamination of high-velocity CO(3-2) emission from the primary nucleus in region B, we can set a lower-limit estimate to the luminosity of the cold molecular gas of $L'_{\text{CO}} \sim 1.3 \text{ K km s}^{-1} \text{ pc}^2$ for region A and $L'_{\text{CO}} \sim 1.4 \text{ K km s}^{-1} \text{ pc}^2$ for region B (see Solomon & Vanden Bout 2005). By adopting a standard conversion factor for ULIRGs of $\alpha_{\text{CO}} = M_{H_2}/L'_{\text{CO}} = 0.8$ (Downes & Solomon 1998), this translates into a conservative estimate of the cold molecular gas of $M_{\text{cold-}H_2} \approx 1.0$ and $1.1 \times 10^7 M_{\odot}$ for region A and B respectively, or $M_{\text{cold-}H_2} \approx 2.1 \times 10^7 M_{\odot}$ in total. Sakamoto et al. (2014) use the CO(1-0) intensity to estimate a total mass of $4.1 \times 10^7 X_{20} M_{\odot}$ for this high-velocity gas (assuming $X_{20} \equiv \frac{N_{H_2}/(1 \times 10^{20})}{I_{\text{CO}(1-0)}}$ and adjusted for our assumed $D=44.6 \text{ Mpc}$ to NGC 3256). Our assumption of $\alpha_{\text{CO}} = 0.8$ translates to $X_{20} \sim 0.4$ (see Bolatto et al. 2013). Therefore, taking into consideration the uncertainties involved regarding contamination of outflowing gas from the primary nucleus, our adopted $\alpha_{\text{CO}} = 0.8$, and the gas thermalization, the

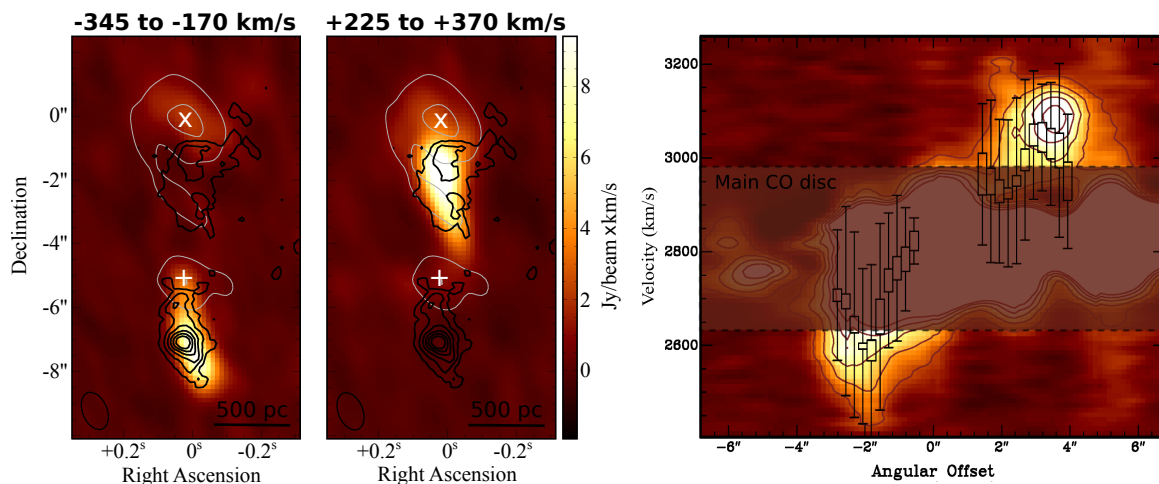


Fig. 6. Total intensity map of the blueshifted (*left*) and redshifted (*middle*) high-velocity CO(3-2) emission in ALMA observations of NGC 3256. The velocity range of the integrated CO(3-2) emission is given in the plots. Overlaid are thick black contours of the broad-component H₂ flux from Fig. 1 (levels from 14% to 80% in steps of 13% of the peak flux), as well as thin gray contours of the 343 GHz radio continuum from the ALMA data (levels at 3 and 10 mJy beam⁻¹; for details see Sakamoto et al. 2014). The relative astrometry between the SINFONI and ALMA data has an estimated uncertainty of $\sim 0.5''$. *Right:* Position-Velocity (PV) diagram of the high-velocity CO(3-2) emission along a north-south direction crossing the secondary nucleus at offset = 0'' (optical velocity definition; contours 20, 40, 60, 80, 100 mJy beam⁻¹). Overlaid are black symbols that represent the broad-component H₂ emission along the same direction (i.e., the NS-aperture from Fig. 1); the box shows the range between the average and maximum value per resolution element ($1.1'' \times 0.25''$), while the error bars indicate $\pm 0.5 \times \text{FWHM}_{\text{average}}$. The complex region of the main CO disk is not discussed (see Sakamoto et al. 2014).

two approaches agree to a mass of at least $M_{\text{cold-H}_2} \sim 2 \times 10^7 M_{\odot}$ of cold molecular gas associated with the broad-component H₂ feature in regions A and B. We will use this value throughout the rest of this paper.

For further details on the CO data we refer to Sakamoto et al. (2014).

4. Discussion

We presented broad-component H₂ emission-line features of hot molecular hydrogen gas in the vicinity of the heavily obscured secondary nucleus of NGC 3256. We here discuss the nature of the broad-component H₂ emission in regions A and B. We present three possible scenarios: a biconical molecular gas outflow, a rotating disk that revolves around the secondary nucleus and a pair of tidal features. We will show that a molecular gas outflow best explains the observed properties (Sect. 4.1). The fact that this outflow is detected at high spatial resolution in both the hot and cold molecular gas phase makes it one of the few molecular outflows for which we can study in detail the physical structure and properties (Sect. 4.2). We will also investigate the driving mechanism of the outflow (Sect. 4.3) and conclude with a brief remark about how our results fit into the broader perspective on molecular gas outflows (Sect. 4.4).

4.1. Nature of the broad-component H₂ emission

The first scenario to explain the broad-component H₂ emission in regions A and B is that of a kpc-scale biconical outflow of molecular gas that originates from the secondary nucleus. We will here show that this scenario explains well the geometry and kinematics of the observed H₂ features. In Fig. 7 we visualize the geometry of the large-scale molecular gas disk and the biconical outflow from the secondary nucleus, as suggested by Sakamoto et al. (2014). The ALMA CO data of Sakamoto et al. (2014) reveal that the large-scale disk has an inclination of $\sim 30^\circ$ and that the southern part of the large-scale disk is the near side if

the tidal-tails are trailing. They also show that the orbital plane of the primary and secondary nucleus must be close to this large-scale gas disk, but that the secondary is in front of the primary core and the secondary's nuclear disk has an inclination of at least $i_{\text{disk}} \sim 70^\circ$. If we assume that the outflow is perpendicular to the nuclear disk, this would render the molecular outflow close to the plane of the sky ($i_{\text{outfl}} \sim 20^\circ$). A biconical molecular gas outflow in a system with this geometry would explain why we see blueshifted H₂ emission in region A and redshifted emission in region B. In addition, the geometry in Fig. 7 suggests that the outflow may interact with the large-scale disk in region A. If this interaction results in shock-heating of molecular gas, this can naturally explain the fact that in region A the enhanced flux of H₂ emission in the outflowing broad-component gas is co-spatial with an enhancement in the H₂ flux of the narrow-component gas disk (Fig. 1). Concluding, the observed geometry and kinematics of the broad-component H₂ emission agree with what is expected from a molecular outflow.

A second scenario is that the broad-component H₂ emission is an edge-on molecular disk or ring that rotates around the secondary nucleus. The velocity dispersion of the broad-component H₂ emission in NGC 3256 is distinctively larger than that of the main gas disk (Sect. 3.1), with $v/\sigma \sim 1.3$. This is intermediate between that of rotation-dominated ($v/\sigma \geq 1$) and random-motion-dominated ($v/\sigma \leq 1$) systems (e.g., Epinat et al. 2012; Bellocchi et al. 2013), suggesting resemblance to a “thick disk”, rather than a classical “thin disk”. However, two arguments make this scenario unlikely. First, the dynamical mass enclosed by this rotating structure would be $M_{\text{dyn}} \approx \frac{v_{\text{rot}}^2 R}{G} \sim 1 \times 10^{10} M_{\odot}$, although following Bellocchi et al. (2013) it could be as high as $M_{\text{dyn}} \approx \frac{2R_{\text{eff}}(v_{\text{rot}}^2 + 1.35\sigma^2)}{G} \sim 3 \times 10^{10} M_{\odot}$ if we take into account the velocity dispersion of the gas (assuming $v_{\text{rot}} = \Delta v_{\text{peak}} = 250 \text{ km s}^{-1}$, $\sigma = 190 \text{ km s}^{-1}$, $R = 700 \text{ pc}$ and $G = 6.67 \times 10^{-11} \text{ m}^3 \text{ kg}^{-1} \text{ s}^{-2}$ the gravitational constant; Table 1). This would result in a gas mass to dynamical mass ratio of $M_{\text{gas}}/M_{\text{dyn}} \approx 1/500 - 1/1500$. This is two orders of magnitude below the typical value of

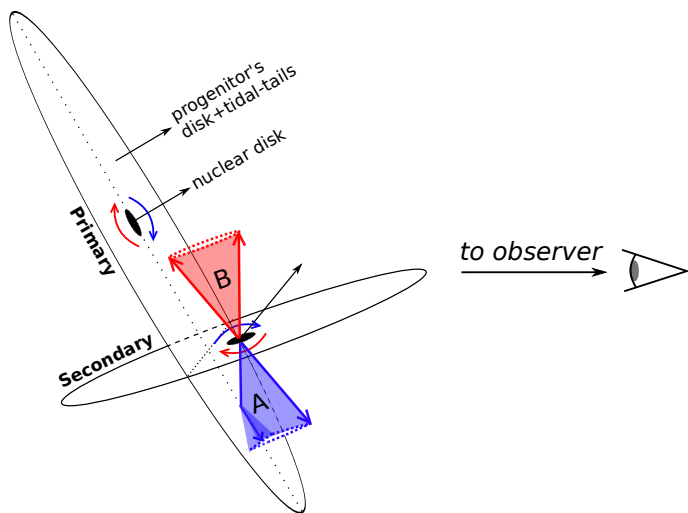


Fig. 7. Alignment between the (nuclear) disks of the progenitor galaxies associated with the primary/secondary nucleus and the H_2 outflow. The alignment of the nuclear disks is based on CO observations by Sakamoto et al. (2014). Simplistically, the large-scale disks and tidal tails of the progenitor galaxies are assumed to be aligned parallel to the nuclear disks.

$M_{\text{gas}}/M_{\text{dyn}} \approx 1/6$ observed for the main central molecular gas disks of ULIRGs (Downes & Solomon 1998). Second, a rotating disk or ring would cross the large-scale primary disk, which would trigger cloud-cloud collisions that would make the structure very unstable and short-lived. We thus argue that a rotating disk or ring is not a likely alternative explanation for the broad-component H_2 emission in regions A and B.

A third scenario is that the broad-component H_2 emission in regions A and B represents tidal features that are not in dynamical equilibrium. The complex kinematics observed within NGC 3256 make this an attractive alternative scenario to investigate. The interaction between the putative tails and the ISM in regions A and B could increase the velocity dispersion of the gas within the tails. However, the observed broad-component features in regions A and B are only detected in the molecular gas phase and have no clear stellar or dusty counterparts, as would be expected for tidal tails (Fig. 3). In addition, the spatial and kinematic geometry of the broad-component structure with respect to the secondary nucleus strongly suggests that the tidal gas would have been stripped off the secondary's central disk. However, Sakamoto et al. (2014) show that the merger orbital plane is close to face-on and they therefore argue that the tidal force between the primary and secondary nucleus cannot produce large line-of-sight velocities for gas that is stripped off the secondary's central disk. Thus, the currently available data do not seem to favor the scenario that the broad-component H_2 emission reflects tidal features.

4.2. Detailed physical properties of the outflow

In Sect. 4.1 we argued that a biconical molecular gas outflow best explains the observed properties of the broad-component H_2 emission in regions A and B. The high spatial resolution of our data reveals interesting physical properties of the outflow. From the narrow width of the H_2 outflow in EW-direction ($\lesssim 300\text{pc}$), our data indicate that the outflow has an opening angle of $\sim 40^\circ$. The highest-velocity H_2 gas is found 440 (800) pc south (north) of the secondary nucleus. This suggests that the molecular outflow peaks far from the nucleus, possibly resembling a biconical

shell-like geometry, with the lower-velocity molecular gas found down-stream of this shell.

The hot-to-cold molecular gas mass ratio of the outflowing gas is $\sim 6 \times 10^{-5}$, which is at the high end of the range $10^{-7} - 10^{-5}$ observed across a sample of several dozen star-forming galaxies and AGN by Dale et al. (2005). Moreover, H_2 has a short cooling timescale of $\sim 10^4$ yr, which is two orders of magnitude shorter than the gas outflow timescale that we will calculate below ($t_{\text{outfl}} \sim 10^6$ yr). This suggests that molecular gas in the outflow may be continuously shocked or heated (as is also observed to be the case for a molecular outflow from the radio-loud ULIRG PKS 1345+12; Dasyra et al. 2014.) The fact that the outflow appears to be predominantly molecular (Sect. 3.1) suggests that the gas is most likely entrained in a wind from the AGN/starburst region, possibly by dragging molecular gas out of the secondary's circum-nuclear disk. This gas is likely heated through relatively slow shocks or X-rays (potentially from the AGN) to our observed temperature of ~ 1900 K. It is not immediately apparent that the H_2 emission could represent a transient phase of gas-cooling after fast shocks accelerate and heat/ionize gas directly at the shock-front (as appears to happen in the nearby active galaxy IC 5063; Tadhunter et al. 2014), because we do not see evidence of copious amounts of ionized gas in Bry that one would expect to be created by such fast shocks.

In Sect. 3.1 we found that the kinematic signature of the outflowing H_2 gas has an observed FWZI ≈ 1200 km s^{-1} , which means that the molecular gas in the outflow reaches a maximum line-of-sight velocity of ± 600 km s^{-1} . If we follow the outflow geometry described in Sect. 4.1 and Fig. 7, with $i_{\text{outfl}} \sim 20^\circ$, this means that the intrinsic outflow velocities can reach a maximum of about ± 1800 km s^{-1} . Similarly, if we assume our observed average outflow velocity to be $v_{\text{avg}} = 0.5 \times \text{FWHM}_{\text{tot}} \approx 280$ km s^{-1} , this translates into an intrinsic average velocity of $v_{\text{avg}} \sim 280 \sin^{-1}(i_{\text{outfl}}) \sim 820$ km s^{-1} . If we also de-project the outflow radius to $R = 700 \cos^{-1}(i_{\text{outfl}}) \sim 750$ pc, this means that it would take the gas roughly 10^6 yr to travel this distance. We note that Sakamoto et al. (2014) argue that the inclination of the outflow axis could even be as low as $i_{\text{outfl}} \sim 5^\circ$, which would increase the above mentioned intrinsic outflow velocities with a factor of ~ 4 . Sakamoto et al. (2014) base this low value for i_{outfl} on the fact that blue- and redshifted CO emission are observed to be co-spatial within the conical outflow, which they argue means that the inclination of the outflow is less than half the opening angle of $\sim 20^\circ$ that they measure from their CO data (i.e., $i_{\text{outflow}} \leq 10^\circ$). However, this does not take into account the large velocity dispersion that we measure for the H_2 gas, which could explain the co-spatial red- and blueshifted emission even when $i_{\text{outfl}} > 10^\circ$. In addition, we find an opening angle for the outflow of $\sim 40^\circ$, larger than the $\sim 20^\circ$ that Sakamoto et al. (2014) derived from the CO data. We therefore argue that $i_{\text{outfl}} < 20^\circ$ is not required to explain the observed properties of the molecular outflow.

With an intrinsic $v_{\text{avg}} \sim 820$ km s^{-1} , $R \sim 750$ pc and a total molecular gas mass of $\sim 2 \times 10^7 M_\odot$ involved in the outflow, the average mass outflow rate is $\dot{M}_{\text{outfl}} \sim 20 M_\odot \text{yr}^{-1}$. This is similar to that of other molecular outflows observed in low- z starburst galaxies and AGN (e.g., Alatalo et al. 2011; Morganti et al. 2013b; Ciccone et al. 2014; Garcia-Burillo et al. 2014, see also Sect. 1). This value for \dot{M}_{outfl} is likely a lower limit, because our estimate of \dot{M}_{outfl} is based on the over-simplified assumption that the total gas mass is driven out in a single event. As we discussed above, it is possible that the outflow is shell-like, or at least continuously re-filled with outflowing clouds, in which case \dot{M}_{out} can be larger by at least a factor of a few (see Maiolino et al.

2012; Ciccone et al. 2014). Still, $\dot{M}_{\text{outfl}} \sim 20 M_{\odot} \text{ yr}^{-1}$ is high compared to the star-formation rate of the secondary nucleus. Following to Kotilainen et al. (1996) and Piqueras López (2014), the star-formation rate in the secondary nucleus is $\text{SFR} \sim 1 - 3 M_{\odot} \text{ yr}^{-1}$ (corrected for estimated extinctions of $A_V \sim 10 - 12$ mag). Although significant uncertainty remains in these estimates, the mass-loading factor could be as high as $\eta = \dot{M}_{\text{out}}/\text{SFR} \sim 10$.

4.3. Outflow mechanism: AGN vs. starburst

The relatively high mass loading factor of the outflow ($\eta = \dot{M}_{\text{out}}/\text{SFR} \sim 10$) indicates that there is a discrepancy between the mass outflow rate and star-formation rate. A similar result on a molecular outflow in the nearby Seyfert galaxy NGC 1068 led Garcia-Burillo et al. (2014) to favor AGN activity over star formation as the likely mechanism to drive the outflow (based on work by Murray et al. 2005 and Veilleux et al. 2005). Moreover, the morphology of the H_2 outflow from the secondary nucleus in NGC 3256 reveals that the outflow is rather collimated with an opening angle of $\sim 40^\circ$, while the intrinsic maximum outflow velocity is high ($v_{\text{max}} \sim 1800 \text{ km s}^{-1}$). Arribas et al. (2014) show that AGN in (U)LIRGs generate ionized gas outflows that are twice as fast as those produced by starbursts in these systems. These results could suggest that a hidden AGN may contribute to driving the outflow, for example through radiation pressure or a magnetically driven accretion-disk wind (e.g., Everett 2005; Proga 2007). Sakamoto et al. (2014) also show marginal evidence for the presence of a faint two-sided radio-jet emanating from the secondary nucleus, which appears to be aligned with the high-velocity CO(3-2) emission (based on data from Neff et al. 2003). Still, unambiguous observational evidence for the presence of an AGN in the secondary nucleus is currently lacking (Sect. 1). So are at least the energetics of the outflow consistent with the scenario that a hidden AGN, or else the nuclear starburst, can drive the outflow?

The combined turbulent and bulk kinetic energy of the molecular outflow,

$$E_{\text{tot}} = E_{\text{kin}}^{\text{turb}} + E_{\text{kin}}^{\text{bulk}} = \frac{3}{2} \cdot M\sigma^2 + \frac{1}{2} \cdot M[v/\sin(i_{\text{outfl}})]^2, \quad (2)$$

is $E_{\text{tot}} \sim 2 \times 10^{56} \text{ erg}$ (for $M \approx 2 \times 10^7 M_{\odot}$, $\sigma \approx 190 \text{ km s}^{-1}$, $v \approx 280 \text{ km s}^{-1}$ and $i_{\text{outfl}} = 20^\circ$). We first compare this to the radiation from a potential AGN accretion disk. The 0.5 – 10 keV X-ray luminosity from the secondary nucleus is $L_X \sim 3 \times 10^{40} \text{ erg s}^{-1}$ (assuming a power-law spectral model with $\Gamma = 2.0$ and an absorbing column of $5 \times 10^{22} \text{ cm}^{-2}$; Lira et al. 2002). Elvis et al. (1994) show that QSOs with $L_{1-10 \text{ keV}} \sim 10^{43-47} \text{ erg s}^{-1}$ have a bolometric luminosity L_{bol} that is 5 – 50 \times larger than $L_{1-10 \text{ keV}}$, with an average/median value of $L_{\text{bol}}/L_{1-10 \text{ keV}} \sim 20$. Ho (2008) estimate a similar value of $L_{\text{bol}}/L_{2-10 \text{ keV}} \sim 16$ for low-luminosity AGN. Lira et al. (2002) show that most of the 0.5 – 10 keV X-ray emission from the secondary nucleus of NGC 3256 occurs in the hard 2 – 10 keV regime, so if we simplistically assume that the X-ray emission comes from a hidden AGN and we apply $L_{\text{bol}}/L_X \sim 16$, then the bolometric AGN luminosity would be $L_{\text{bol}} \sim 5 \times 10^{41} \text{ erg s}^{-1}$ in case the AGN would be X-ray-transparent or Compton-thin. Over the outflow timescale of 10^6 yr , the total energy deposited by the AGN would be $\sim 2 \times 10^{55} \text{ erg s}^{-1}$, an order of magnitude too low to drive the outflow. However, if the X-ray emission is scattered emission from a Compton-thick (i.e., X-ray-obscured) AGN, the AGN's intrinsic L_X , and thus also L_{bol} , can be a factor of 60 – 70 higher (Panessa et al. 2006; Singh et al. 2011). The non-detection of the Fe α line at 6.4 keV has led Pereira-Santaella et al. (2011)

to conclude that the upper limit to L_{bol} for a Compton-thick AGN is on the order of $10^{43} \text{ erg s}^{-1}$ in NGC 3256. Still, when adopting this upper limit, it would imply that a Compton-thick AGN, in case it has remained active over the past $\sim 10^6 \text{ yr}$, may have released a total energy of up to $\sim 3 \times 10^{56} \text{ erg s}^{-1}$ over this period, which would have been sufficient to drive the outflow.

How about mechanical energy from the putative radio source? As shown by Sakamoto et al. (2014, their Fig. 19), the weak radio source appears to have a two-sided jet with a total 8 GHz radio flux of at most $F_{8 \text{ GHz}} \sim 1 \text{ mJy}$ (i.e., not taking into account the nuclear emission). From the flux of the jet we can derive the bulk kinetic power of the radio source by following Willott et al. (1999) and Godfrey & Shabala (2013):

$$Q_{\text{jet}} \approx f^{3/2} 3 \times 10^{38} \left(\frac{L_{151 \text{ MHz}}}{10^{28} \text{ W Hz}^{-1} \text{ sr}^{-2}} \right) \text{ W}, \quad (3)$$

where $L_{151 \text{ MHz}}$ is the 151 MHz luminosity (derived from the 151 MHz flux and luminosity distance through $L_{151 \text{ MHz}} = F_{151} D_L^2$) and f is a factor that represents errors in the model assumption, including the excess energy in particles compared with that in the magnetic field, geometrical effects and energy in the backflow of the lobe (see Willott et al. 1999 and Blundell & Rawlings 2000 for details). Following Blundell & Rawlings (2000), the value of f is typically around 10 – 20, so here we assume $f = 15$. In the optimistic case that the jet has a steep radio spectrum with $S_\nu \propto \nu^{-1}$, thus $F_{151} \sim 55 \text{ mJy}$, we estimate that $Q_{\text{jet}} \sim 2 \times 10^{40} \text{ erg s}^{-1}$. Over a typical radio-source lifetime of 10^6 yr , the mechanical energy deposited by the radio source would only be on the order of $\sim 6 \times 10^{53} \text{ ergs}$. This is two orders of magnitude lower than the combined turbulent and bulk kinetic energy of the molecular outflow, which suggests that the putative radio source currently does not have the power that is required to drive the outflow. Still, the presence of a radio source carving its way through the ISM may potentially have aided in creating a cavity through which molecular gas can be efficiently accelerated.

Alternatively, can the necessary energy for driving the outflow be injected by a nuclear starburst? Kotilainen et al. (1996) and Norris & Forbes (1995) derive a supernova-rate in the secondary nucleus of $R_{\text{SN}} \sim 0.3 \text{ SN yr}^{-1}$. Assuming an energy-release per supernova event of $\sim 10^{51} \text{ erg}$ (Bethe & Pizzochero 1990), and the fact that up to 90% of the energy per supernova is likely radiated away (Thornton et al. 1998), the total energy deposited into the ISM by supernovae over the course of the outflow timescale t_{outfl} is roughly

$$E_{\text{SN}} = 10^{51} \cdot \epsilon \cdot R_{\text{SN}} \cdot t_{\text{outfl}} \text{ (erg)}, \quad (4)$$

with ϵ the assumed efficiency of energy transfer to the ISM. For $R_{\text{SN}} \sim 0.3 \text{ SN yr}^{-1}$, $\epsilon \sim 0.1$ and $t_{\text{outfl}} \sim 10^6 \text{ yr}$, the energy-deposition by supernovae is $E_{\text{SN}} = 3 \times 10^{55} \text{ ergs}$. Stellar winds will release additional energy into the system, although Leitherer et al. (1992) show that once the starburst has aged enough that supernova-explosions occur, stellar winds will increase the total energy deposited into the ISM by at most a factor of 2, putting a limit of $E_{\text{SN}+\text{winds}} \sim 6 \times 10^{55} \text{ ergs}$. This is only a factor of 3 lower than the energy of the outflow. Given the assumptions involved, and the fact that it is uncertain to what extent the large amounts of radiative energy may contribute to driving the outflow, it is possible that the energy output of the starburst event in the secondary nucleus may be sufficient to sustain the outflow.

Concluding, the high mass loading factor, high outflow velocities and substantial collimation of the outflow suggest that that a hidden AGN may contribute to driving the outflow of

molecular gas from the secondary nucleus. Based on the energetics, we argue that the most plausible way a hidden AGN can drive the outflow is in the Compton-thick regime, through radiation-pressure or an accretion-disk wind. However, the scenario that the nuclear starburst provides the energy needed to drive the outflow is also possible.

4.4. Broader perspective

Interestingly, while the biconical structure of the outflow shows a distinct blue- and redshifted wing to the emission-line profile on either side of the secondary nucleus, when integrated across the entire outflow region the broad-component profile appears symmetric with respect to the assumed systemic velocity of the secondary nucleus (Fig. 2). This is similar to what is often seen in CO data with much lower spatial resolution, and for objects at intermediate- and high- z (e.g., Feruglio et al. 2010; Maiolino et al. 2012; Cicone et al. 2014). Thus, our results provide valuable insight into understanding the structural properties of starburst/AGN-driven molecular gas outflows in general.

5. Conclusions

We presented evidence for the presence of a kpc-scale biconical outflow of hot molecular gas from the heavily obscured secondary nucleus of NGC 3256, based on near-IR $2.12\mu\text{m}$ H_2 data obtained with VLT/SINFONI. Our main conclusions are:

i). The outflow is observed at high spatial resolution in both the hot molecular gas phase with VLT/SINFONI (H_2) and the cold molecular phase with ALMA (CO). The hot and cold component of the molecular outflow share a similar morphology and kinematics.

ii). These data allowed us to characterize the geometry, kinematics and physical properties of the molecular outflow. In particular:

- The outflow consists of a blueshifted outflow-component south and a redshifted component north of the secondary nucleus, with an opening angle of $\sim 40^\circ$;
- The emission-line kinematics show observed maximum outflow velocities of $\pm 600 \text{ km s}^{-1}$. However, given the low inclination of the jet-axis ($i_{\text{outfl}} \sim 20^\circ$), intrinsic outflow velocities can reach a maximum of $\sim 1800 \text{ km s}^{-1}$;
- The mass of the hot molecular gas in the outflow is $M_{\text{hotH}_2} \sim 1200 M_\odot$, while the outflowing cold molecular gas mass is $M_{\text{coldH}_2} \sim 2 \times 10^7 M_\odot$. This results in a hot-to-cold molecular gas mass ratio of $\sim 6 \times 10^{-5}$ and total molecular mass-outflow rate of at least $\dot{M}_{\text{outfl}} \sim 20 M_\odot \text{ yr}^{-1}$;
- From the analysis of multiple near-IR H_2 -transitions, we derive a temperature of $T \sim 1900 \pm 300 \text{ K}$ for the hot H_2 gas in the outflow. The likely heating mechanism is either shocks or X-ray emission.

iii). A likely driving mechanism for the molecular outflow is a hidden AGN, given the high mass-loading factor ($\eta \sim 10$), high outflow velocities and significant collimation of the outflowing gas. Based on energy requirements, this would most likely happen in the Compton-thick regime, through radiation pressure or an accretion-disk wind. Alternatively, the nuclear starburst may potentially provide enough energy to drive the outflow;

iv). When integrated over the outflow region, the global kinematics of the outflowing molecular gas mimic those observed with

low-resolution CO observations in other low- and high- z objects. The structural and physical properties of the molecular outflow in NGC 3256 that we derive from our high-resolution data therefore provide valuable insight into our general understanding of starburst/AGN-driven molecular gas outflows.

Acknowledgements. We thank the anonymous referee for valuable suggestions that substantially improved the content of this paper. BE is grateful that the research leading to these results has received funding from the Spanish Ministerio de Economía y Competitividad (MINECO) under grant AYA2010-21161-C02-01 and from the European Union Seventh Framework Programme (FP7-PEOPLE-2013-IEF) under grant agreement n° 624351. LC, SA and AAH acknowledge support through MINECO grants AYA-2012-39408-C02-01 and AYA-2012-31447. MPS is supported by the Agenzia Spaziale Italiana (ASI), contract I/005/11/0. Based on observations collected at the European Organisation for Astronomical Research in the Southern Hemisphere, Chile, prog. 078.B-0066A. The Atacama Large Millimeter Array (ALMA), an international astronomy facility, is a partnership of Europe, North America and East Asia in cooperation with the Republic of Chile. Based on observations made with the NASA/ESA Hubble Space Telescope, and obtained from the Hubble Legacy Archive, which is a collaboration between the Space Telescope Science Institute (STScI/NASA), the Space Telescope European Coordinating Facility (ST-ECF/ESA) and the Canadian Astronomy Data Centre (CADC/NRC/CSA).

Appendix A: Properties H_2 transitions

In this Appendix we provide the spectra and line fluxes derived from fitting two Gaussian components to the emission-line spectra of the various H_2 transitions in regions A, B and C.

Appendix A.1: Method

For each of the seven H_2 transition in our SINFONI data we extracted an emission-line spectrum from a circular aperture of 13 spaxels centered around the peak flux in regions A, B and C (similar to what is shown in Fig. 1 for H_2 1-0 S(1)).

As mentioned in Sect. 2, we used an IDL routine based on the MPFIT package to perform the line-fitting. We used a three-component model to simultaneously fit the continuum and both the narrow and broad component of the emission lines. The continuum was fitted using a linear term, whereas a Gaussian profile was used for each emission-line component.

As can be seen in Fig. A.1, the signal-to-noise of some of the lines is too low to derive accurate results when using this multi-component analysis without placing any constraints on the line-fitting procedure. To reduce the uncertainties of the fitting and obtain more robust measurements of the line fluxes, we assumed that all transitions share the same kinematics. We first performed the fitting routine on the strong 1-0 S(1) $2.1218\mu\text{m}$ line without placing constraints on the line-fitting parameters. Subsequently, we used these results to fix the position and line width (both in km s^{-1}) of the narrow and broad component of the other emission lines.

The uncertainties of the flux measurements were calculated using a Monte Carlo technique. This method consists of measuring the noise in the spectra as the root-mean-square of the residuals after the subtraction of our multi-component model. Taking this estimation of the noise into account, we construct a total of 500 independent simulations/realizations of the spectra, where the lines are again fitted. These simulations yield distributions of each free parameter of our model. The uncertainty of each parameter is then defined as the standard deviation of its corresponding distribution.

Appendix A.2: Results

In Fig. A.1 we show the results of the line-fitting procedure. In Table A.1 we summarize the line ratios for the broad and narrow component with respect to the flux of the 1-0 S(1) 2.1218 μm line. The upper limits are defined as 1-sigma detections, using the noise estimation from the Monte Carlo method described in Sect. A.1.

References

- Aalto, S., Booth, R. S., Johansson, L. E. B., & Black, J. H. 1991, *A&A*, 247, 291
Aalto, S., Muller, S., Sakamoto, K., et al. 2012, *A&A*, 546, A68
Alatalo, K., Blitz, L., Young, L. M., et al. 2011, *ApJ*, 735, 88
Alonso-Herrero, A., Pereira-Santaella, M., Rieke, G. H., & Rigopoulou, D. 2012, *ApJ*, 744, 2
Alonso-Herrero, A., Colina, L., Packham, C., et al. 2006a, *ApJL*, 652, L83
Alonso-Herrero, A., Rieke, G. H., Rieke, M. J., et al. 2006b, *ApJ*, 650, 835
Arribas, S., Colina, L., Bellocchi, E., Maiolino, R., & Villar-Martín, M. 2014, *A&A*, 568, 14
Baan, W. A., Henkel, C., Loenen, A., et al. 2008, *A&A*, 477, 747
Bedregal, A. G., Colina, L., Alonso-Herrero, A., & Arribas, S. 2009, *ApJ*, 698, 1852
Bellocchi, E., Arribas, S., Colina, L., Miralles-Caballero, D. 2013, *A&A*, 557, 59
Bethe, H. A. & Pizzochero, P. 1990, *ApJL*, 350, L33
Black, J. H. & van Dishoeck, E. F. 1987, *ApJ*, 322, 412
Blundell, K. M. & Rawlings, S. 2000, *AJ*, 119, 1111
Bolatto, A. D., Wolfire, M., & Leroy, A. K. 2013, *ARA&A*, 51, 207
Bonnet, H., Abuter, R., Baker, A., et al. 2004, *The Messenger*, 117, 17
Brand, P. W. J. L., Toner, M. P., Geballe, T. R., et al. 1989, *MNRAS*, 236, 929
Casoli, F., Dupraz, C., & Combes, F. 1992, *A&A*, 264, 49
Cazzoli, S., Arribas, S., Colina, L., et al. 2014, (arXiv/1406.5154)
Chung, A., Yun, M. S., Narayanan, G., Heyer, M., & Erickson, N. R. 2011, *ApJL*, 732, L15
Cicone, C., Maiolino, R., Sturm, E., et al. 2014, *A&A*, 562, A21
Combes, F., García-Burillo, S., Casasola, V., et al. 2013, *A&A*, 558, A124
Dale, D., Sheth, K., Helou, G., Regan, M., Hüttemeister, S. 2005, *AJ*, 129, 2197
Dasyra, K. M. & Combes, F. 2012, *A&A*, 541, L7
Dasyra, K. M., Combes, F., Novak, G. S., et al. 2014, *A&A*, 565, A46
Davies, R. I., Sternberg, A., Lehnert, M., & Tacconi-Garman, L. E. 2003, *ApJ*, 597, 907
Díaz-Santos, T., Alonso-Herrero, A., Colina, L., et al. 2008, *ApJ*, 685, 211
Dors, Jr., O. L., Riffel, R. A., Cardaci, M. V., et al. 2012, *MNRAS*, 422, 252
Downes, D. & Solomon, P. M. 1998, *ApJ*, 507, 615
Doyon, R., Joseph, R. D., & Wright, G. S. 1994, *ApJ*, 421, 101
Draine, B. T. & Woods, D. T. 1990, *ApJ*, 363, 464
Eisenhauer, F., Abuter, R., Bickert, K., et al. 2003, in *SPIE Conference Series*, Vol. 4841, ed. M. Iye & A. F. M. Moorwood, 1548–1561
Elvis, M., Wilkes, B. J., McDowell, J. C., et al. 1994, *ApJS*, 95, 1
English, J., Koribalski, B., Bland-Hawthorn, J., Freeman, K. C., & McCain, C. F. 2010, *AJ*, 139, 102
Epinat, B., Tasca, L., Amram, P., et al. 2012, *A&A*, 539, A92
Everett, J. E. 2005, *ApJ*, 631, 689
Falcón-Barroso, J., Ramos Almeida, C., Böker, T., et al. 2014, *MNRAS*, 438, 329
Feruglio, C., Maiolino, R., Piconcelli, E., et al. 2010, *A&A*, 518, L155
García-Burillo, S., Combes, F., Usero, A., et al. 2014, *A&A*, 567, 125
Godfrey, L. E. H. & Shabala, S. S. 2013, *ApJ*, 767, 12
Guillard, P., Ogle, P. M., Emonts, B. H. C., et al. 2012, *ApJ*, 747, 95
Heckman, T. M., Armus, L., & Miley, G. K. 1990, *ApJS*, 74, 833
Heckman, T. M., Lehnert, M., Strickland, D., & Armus, L. 2000, *ApJS*, 129, 493
Ho, L. C. 2008, *ARA&A*, 46, 475
Hollenbach, D. & McKee, C. F. 1989, *ApJ*, 342, 306
Jenkins, L. P., Roberts, T. P., Ward, M. J., & Zezas, A. 2004, *MNRAS*, 352, 1335
Kotilainen, J. K., Moorwood, A., Ward, M., & Forbes, D. 1996, *A&A*, 305, 107
Laine, S., van der Marel, R. P., Rossa, J., et al. 2003, *AJ*, 126, 2717
Leitherer, C., Robert, C., & Drissen, L. 1992, *ApJ*, 401, 596
Leitherer, C., Chandar, R., Tremonti, C. A., Wofford, A., & Schaerer, D. 2013, *ApJ*, 772, 120
Leon, S., Eckart, A., Laine, S., et al. 2007, *A&A*, 473, 747
Lepp, S. & McCray, R. 1983, *ApJ*, 269, 560
Lípari, S., Díaz, R., Taniguchi, Y., et al. 2000, *AJ*, 120, 645
Lípari, S. L., Díaz, R. J., Forte, J. C., et al. 2004, *MNRAS*, 354, L1
Lira, P., Gonzalez-Corvalan, V., Ward, M., & Hoyer, S. 2008, *MNRAS*, 384, 316
Lira, P., Ward, M., Zezas, A., Alonso-Herrero, A., & Ueno, S. 2002, *MNRAS*, 330, 259
Mahony, E. K., Morganti, R., Emonts, B. H. C., Oosterloo, T. A., & Tadhunter, C. 2013, *MNRAS*, 435, L58
Maiolino, R., Gallerani, S., Neri, R., et al. 2012, *MNRAS*, 425, L66
Maloney, P. R., Hollenbach, D. J., & Tielens, A. G. G. M. 1996, *ApJ*, 466, 561
Markwardt, C. B. 2009, *ASP Conference Series*, Volume 411, ed. D. A. Bohlander, D. Durand, & P. Dowler, 251
Mazzalay, X., Saglia, R. P., Erwin, P., et al. 2013, *MNRAS*, 428, 2389
Mirabel, I. F., Booth, R. S., Johansson, L. E. B., Garay, G., & Sanders, D. B. 1990, *A&A*, 236, 327
Monreal-Ibero, A., Arribas, S., Colina, L., et al. 2010, *A&A*, 517, A28
Moorwood, A. F. M. & Oliva, E. 1994, *ApJ*, 429, 602
Moran, E. C., Lehnert, M. D., & Helfand, D. J. 1999, *ApJ*, 526, 649
Morganti, R., Oosterloo, T. A., Tadhunter, C. N., van Moorsel, G., & Emonts, B. 2005, *A&A*, 439, 521
Morganti, R., Fogasy, J., Paragi, Z., Oosterloo, T., & Orienti, M. 2013a, *Science*, 341, 1082
Morganti, R., Frieswijk, W., Oonk, R. J. B., Oosterloo, T., & Tadhunter, C. 2013b, *A&A*, 552, L4
Mouri, H. 1994, *ApJ*, 427, 777
Murray, N., Quataert, E., & Thompson, T. A. 2005, *ApJ*, 618, 569
Neff, S. G., Ulvestad, J. S., & Campion, S. D. 2003, *ApJ*, 599, 1043
Norris, R. P. & Forbes, D. A. 1995, *ApJ*, 446, 594
Oosterloo, T. A., Morganti, R., Tzioumis, A., et al. 2000, *AJ*, 119, 2085
Panessa, F., Bassani, L., Cappi, M., et al. 2006, *A&A*, 455, 173
Pereira-Santaella, M., Alonso-Herrero, A., Rieke, G. H., et al. 2010, *ApJS*, 188, 447
Pereira-Santaella, M., Alonso-Herrero, A., Santos-Lleo, M., et al. 2011, *A&A*, 535, A93
Piqueras López, 2014, PhD Thesis, Universidad Complutense Madrid
Piqueras López, J., Colina, L., Arribas, S., Alonso-Herrero, A. 2013, *A&A*, 553, 85
Piqueras López, J., Colina, L., Arribas, S., Alonso-Herrero, A., & Bedregal, A. G. 2012a, *A&A*, 546, A64
Piqueras López, J., Davies, R., Colina, L., & Orban de Xivry, G. 2012b, *ApJ*, 752, 47
Proga, D. 2007, in *Astronomical Society of the Pacific Conference Series*, Vol. 373, *The Central Engine of Active Galactic Nuclei*, ed. L. C. Ho & J.-W. Wang, 267
Ramos Almeida, C., Pérez García, A. M., & Acosta-Pulido, J. A. 2009, *ApJ*, 694, 1379
Rich, J. A., Kewley, L. J., Dopita, M. A. 2011, *ApJ*, 734, 87
Riffel, R., Rodríguez-Ardila, A., Aleman, I., et al. 2013, *MNRAS*, 430, 2002
Rodríguez-Zaurín, J., Arribas, S., Monreal-Ibero, A., et al. 2011, *A&A*, 527, A60
Rodríguez Zaurín, J., Tadhunter, C. N., Rose, M., & Holt, J. 2013, *MNRAS*, 432, 138
Rossa, J., Laine, S., van der Marel, R. P., et al. 2007, *AJ*, 134, 2124
Rupke, D. S. N. & Veilleux, S. 2011, *ApJ*, 729, L27
Rupke, D. S. N. & Veilleux, S. 2013, *ApJL*, 775, L15
Sakamoto, K., Aalto, S., Combes, F., Evans, A., & Peck, A. 2014, submitted to *ApJ* (arXiv/1403.7117)
Sakamoto, K. 2013a, in *ASP Conference Series*, Vol. 477, ed. W.-H. Sun, C. K. Xu, N. Z. Scoville, & D. B. Sanders, 21
Sakamoto, K. 2013b, in *IAU Symp.*, Vol. 292, ed. T. Wong & J. Ott, 143, 148
Sakamoto, K., Ho, P. T. P., & Peck, A. B. 2006, *ApJ*, 644, 862
Sanders, D., Mazzarella, J., Kim, D., Surace, J., Soifer, B. 2003, *AJ*, 126, 1607
Sanders, D. B. & Mirabel, I. F. 1996, *ARA&A*, 34, 749
Sargent, A. I., Sanders, D. B., & Phillips, T. G. 1989, *ApJL*, 346, L9
Scarrott, S. M., Draper, P. W., & Stockdale, D. P. 1996, *MNRAS*, 279, 1325
Scoville, N. Z., Hall, D., Ridgway, S., & Kleinmann, S. 1982, *ApJ*, 253, 136
Singh, V., Shastri, P., & Risaliti, G. 2011, *A&A*, 533, A128
Solomon, P. M. & Vanden Bout, P. A. 2005, *ARA&A*, 43, 677
Spoon, H. W. W., Farrah, D., Leboutteiller, V., et al. 2013, *ApJ*, 775, 127
Sternberg, A. & Dalgarno, A. 1989, *ApJ*, 338, 197
Sturm, E., González-Alfonso, E., Veilleux, S., et al. 2011, *ApJL*, 733, L16
Tadhunter, C., Morganti, R., Rose, M., Oonk, J. B. R., & Oosterloo, T. 2014, *Nature*, 511, 440
Tanaka, M., Hasegawa, T., Hayashi, S. S., Brand, P. W. J. L., & Gatley, I. 1989, *ApJ*, 336, 207
Thornton, K., Gaudlitz, M., Janka, H.-T., & Steinmetz, M. 1998, *ApJ*, 500, 95
Veilleux, S., Cecil, G., & Bland-Hawthorn, J. 2005, *ARA&A*, 43, 769
Veilleux, S., Meléndez, M., Sturm, E., et al. 2013, *ApJ*, 776, 27
Westmoquette, M. S., Clements, D. L., Bendo, G. J., & Khan, S. A. 2012, *MNRAS*, 424, 416
Willott, C. J., Rawlings, S., Blundell, K. M., & Lacy, M. 1999, *MNRAS*, 309, 1017
Zepf, S. E., Ashman, K. M., English, J., Freeman, K. C., & Sharples, R. M. 1999, *AJ*, 118, 752

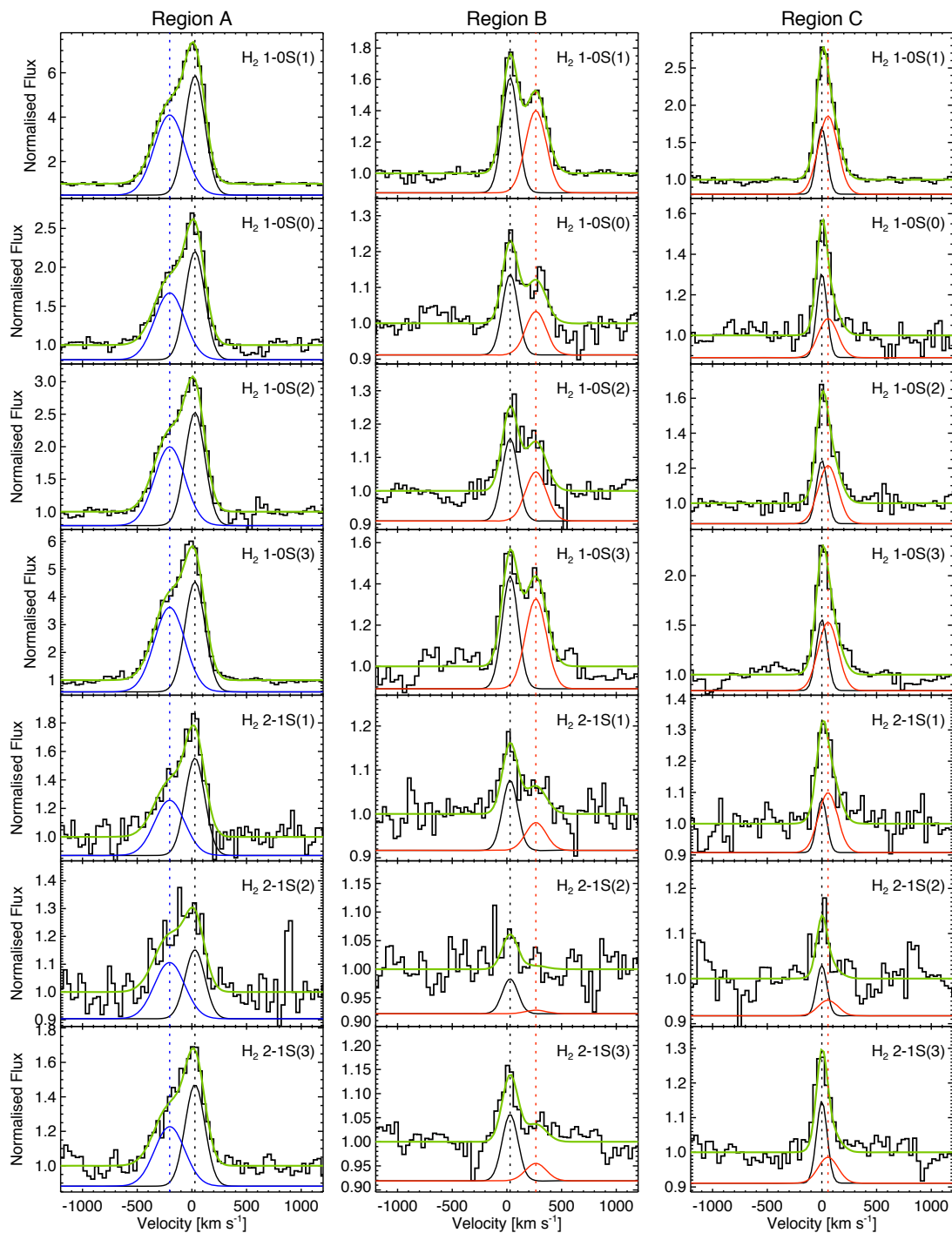


Fig. A.1. Emission-line spectra and 2-component Gaussian fit of the various H_2 transitions in regions A, B and C. The spectra were extracted from a circular aperture of 13 spaxels, centered on the broad-component H_2 feature in each region. The line width and shift between the peak of the narrow and broad component were constrained in velocity to those of the strong 1-0S(1) line. A straight line was fitted to the continuum across a wide velocity range of $-1800 - +1800 \text{ km s}^{-1}$ in order to handle potential features in the continuum (see, e.g., the H_2 1-0S(3) transition in region B). However, a smaller velocity range is plotted in the figures to high-light the details of the fits to the emission lines. After extracting flux measurements, for visualisation purposes the spectra in the plots were normalized to the fitted continuum.

Table A.1. Flux ratios of the broad and narrow components of all seven H₂ lines in our SINFONI data with respect to 1-0 S(1) in regions A, B and C. The absolute flux of the 1-0 S(1) transition is provided at the top.

H ₂ trans.	λ_{rest} (μm)	Broad component			Narrow component		
		Flux 1-0 S(1) ($\times 10^{-16}$ erg s ⁻¹ cm ⁻²)			Flux 1-0 S(1) ($\times 10^{-16}$ erg s ⁻¹ cm ⁻²)		
		A	B	C	A	B	C
1-0 S(1)	2.1218	5.966 \pm 0.306	1.913 \pm 0.188	2.135 \pm 0.399	5.826 \pm 0.297	2.028 \pm 0.175	0.953 \pm 0.403
		Flux ratio with respect to 1-0 S(1)			Flux ratio with respect to 1-0 S(1)		
		A	B	C	A	B	C
1-0 S(0)	2.2235	0.239 \pm 0.014	0.219 \pm 0.033	0.179 \pm 0.046	0.257 \pm 0.014	0.290 \pm 0.032	0.453 \pm 0.197
1-0 S(1)	2.1218	1.000 \pm n.a.	1.000 \pm n.a.	1.000 \pm n.a.	1.000 \pm n.a.	1.000 \pm n.a.	1.000 \pm n.a.
1-0 S(2)	2.0338	0.361 \pm 0.022	0.290 \pm 0.050	0.326 \pm 0.068	0.349 \pm 0.021	0.351 \pm 0.045	0.434 \pm 0.190
1-0 S(3)	1.9576	0.958 \pm 0.052	0.887 \pm 0.103	0.693 \pm 0.147	0.841 \pm 0.045	0.806 \pm 0.082	0.898 \pm 0.396
2-1 S(1)	2.2477	0.109 \pm 0.010	0.113 \pm 0.027	0.175 \pm 0.043	0.128 \pm 0.010	0.203 \pm 0.026	0.181 \pm 0.089
2-1 S(2)	2.1542	0.054 \pm 0.008	<0.067	<0.049	0.045 \pm 0.006	0.080 \pm 0.021	0.123 \pm 0.065
2-1 S(3)	2.0735	0.101 \pm 0.008	0.070 \pm 0.021	0.072 \pm 0.025	0.115 \pm 0.007	0.190 \pm 0.023	0.275 \pm 0.121